Journal of Catalysis 314 (2014) 94–100

Contents lists available at ScienceDirect

Journal of Catalysis

journal homepage: www.elsevier.com/locate/jcat

Chemical imaging of the sulfur-induced deactivation of Cu/ZnO catalyst bodies

Andrew M. Beale [a,b,c,*], Emma K. Gibson [b,c], Matthew G. O'Brien [a], Simon D.M. Jacques [c,d], Robert J. Cernik [d], Marco Di Michiel [e], Paul D. Cobden [f], Özlem Pirgon-Galin [f], Leon van de Water [g], Michael J. Watson [g], Bert M. Weckhuysen [a,*]

[a] Inorganic Chemistry and Catalysis, Debye Institute for Nanomaterials Science, Utrecht University, Universiteitsweg 99, 3584 CG Utrecht, The Netherlands
[b] Department of Chemistry, University College London, 20 Gordon Street, London WC1H 0AJ, UK
[c] UK Catalysis Hub, Research Complex at Harwell, Rutherford Appleton Laboratory, Harwell, Didcot, Oxfordshire OX11 0QX, UK
[d] School of Materials, University of Manchester, Manchester M13 9PL, England, UK
[e] The European Synchrotron Facility, 6 Rue Jules Horowitz, 38000 Grenoble, France
[f] Energy Research Centre of the Netherlands (ECN), Westerduinweg 3, 1755LE Petten, The Netherlands
[g] Johnson Matthey Technology Centre, Billingham, Cleveland TS23 1LB, England, UK

ARTICLE INFO

Article history:
Received 7 January 2014
Revised 1 April 2014
Accepted 6 April 2014
Available online 26 April 2014

Keywords:
Catalyst bodies
Cu/ZnO
Poisoning
X-ray imaging

ABSTRACT

The effects of sulfur poisoning on the water–gas shift (WGS) activity of industrial $Cu/ZnO/Al_2O_3$ catalyst bodies have been studied. The samples were characterized using chemical imaging methods, including XRD-CT, XAFS mapping, and XRF, in order to understand the process by which accelerated sulfur poisoning leads to catalyst deactivation. After ~90 h on stream, all catalysts exhibited reduced activity; the higher the H_2S concentration, the greater the extent of deactivation. Non-invasive XRD-CT measurements performed on intact samples recovered from the reactor revealed the formation of sulfide phases, including sphalerite (β-ZnS) and crystalline CuS, Cu_2S, and $CuSO_4$ phases. These sulfide phases were distributed predominantly as a graduated corona around the sample edge reaching ~1.5 mm thick for experiments performed in the highest concentration of 500 ppm H_2S. XAFS mapping, which is particularly sensitive to the local coordination environment around the element being probed, confirmed the presence of mixed Cu/Zn–O/S coordination environments and that the core of the sample remained sulfur-free. A combination of XRD-CT and XRF revealed that CuS appeared to be mobile under reaction conditions resulting in the redistribution of Cu toward the very edge of the samples. A combination of techniques has therefore demonstrated that H_2S deactivation of $Cu/ZnO/Al_2O_3$ catalyst bodies occurs via phase transformation of the active Cu/ZnO phase into sulfides and redistribution of these components over the sample instead of Cu active site poisoning by S_{ads} species.

1. Introduction

Catalyst deactivation by poisoning, in particular by sulfur (S), is a common problem for a wide range of catalytic processes [1–4]. Examples include the majority of petrochemical processes, methanol synthesis, steam reforming, and selective hydrogenation/dehydrogenations. Such a deactivation is a major problem for the catalyst, resulting in a loss in activity and/or selectivity leading to reduced catalyst lifetimes and increased production costs [4,5]. Strategies to reduce the impact of sulfur poisons typically involve their prior extraction from the process stream via scrubbing. This either involves their adsorption onto a high surface reactive support (e.g., ZnO) or processing with physical and/or chemical solvents [6]. Such technologies are, however, limited in their capacity (even the leading technologies do not completely eliminate sulfur), resulting in variable levels of sulfur-containing poisons passing through the catalytic process, which operates downstream.

There is clearly an economic advantage to be realized by the utilization of catalysts with increased resistance to deactivation by sulfur poisoning. This will become more important as the chemical industry moves from relatively clean feeds, such as natural gas and crude oil, to alternative feedstocks, such as bitumen tars and some

* Corresponding authors. Addresses: Department of Chemistry, University College London, 20 Gordon Street, London WC1H 0AJ, UK and Inorganic Chemistry and Catalysis Group, Debye Institute for Nanomaterials Science, Utrecht University, Universiteitsweg 99, 3584 CG Utrecht, The Netherlands (A.M. Beale).
E-mail addresses: andrew.beale@ucl.ac.uk (A.M. Beale), b.m.weckhuysen@uu.nl (B.M. Weckhuysen).

http://dx.doi.org/10.1016/j.jcat.2014.04.007
0021-9517/

forms of biomass [7]. Such "advantaged" feedstocks are sometimes characterized by higher sulfur levels [8]. Detailed compositions vary with feedstock and from location to location, but some examples of commercially important feedstocks can contain between 1% and 5% sulfur. Catalysts with the ability to resist deactivation and operate in the presence of higher levels of poisons will be required to realize the potential of these new feedstocks [9].

Cu/ZnO catalysts represent the industrial standard for the production of methanol but have also found use in the water–gas shift (WGS) reaction, methanol steam reforming, and methanol decomposition [10–14]. However, they are particularly susceptible to S-poisoning. It is thought that sulfur, in the form of either H_2S or other sulfur compounds, accumulates on Cu-based catalysts leading to blocking of the active site [12,15]. A second problem is that in addition to its structural/catalytic role in Cu/ZnO catalysts, ZnO is also employed as a sulfur trap via the formation of ZnS; it has also been shown that sulfur adsorption is even promoted in the presence of Cu [15]. Higher ZnO content in the catalyst has also been shown to improve S-poisoning tolerance [16,17]. There are two forms of ZnS, namely wurtzite (α-ZnS) and sphalerite (β-ZnS), and both forms are observed in discharged plant samples, although β-ZnS is the more stable form below 1020 °C [18]. Furthermore, $Zn_3O(SO_4)_2$ and $Cu_{1.5}ZnSO_4(OH)_3$ have also been found in deactivated catalysts, indicating that in a commercial reactor, the gas phase is less reducing near the reactor outlet, leading to the sulfate formation (we note, however, that it is not possible to rule out that the sulfate phase formed during a sample passivation process that is typically performed prior to catalyst extraction). In contrast, while some reports exist regarding the observation of CuS, Cu_2S (either polymorph) and/or other members of the chalcocite group where Cu:S lies between 2 and 1 have not been unambiguously determined [19–21]. Surface studies have shown that initially S_{ad} atoms form on Cu surfaces Cu(111/110) via the removal of chemisorbed oxygen, even at low temperatures [22–25].

In an industrial reactor, catalysts are used in pre-shaped forms, i.e., as millimeter-sized catalyst bodies [26]. As such, a study examining deactivation in real catalyst samples needs to consider the problem from a spatial perspective in order to assess quantitatively, macroscopic effects leading to catalyst deactivation, i.e., "shell progressive," "shrinking core," and "pore mouth" effects. To the best of our knowledge, such a spatially resolved systematic study on the S-poisoning of pre-shaped catalyst materials has not previously been performed or is available in the open literature. Therefore, this paper presents the results from a study using both invasive and non-invasive chemical imaging techniques in order to understand the process by which sulfur poisoning leads to a loss in catalytic activity of $Cu/ZnO/Al_2O_3$ catalysts used in the WGS reaction. We demonstrate in particular how techniques, such as XRD-CT, revealed that these catalyst bodies deactivate via the solid-state transformation of the active Cu/ZnO phase(s) into the inactive copper and zinc sulfide phases, respectively [27–30].

2. Experimental

The experiments were performed at station ID15B of the European Synchrotron Research Facility (ESRF, Grenoble, France) using a monochromatic E = 86.88 keV (0.1427 Å) 100 μm square section pencil beam with diffracted X-rays recorded on a Pixium 4700 flat panel detector. Each 2D cross section was recorded at 43 translations spaced 100 μm across the body each with 30 rotations of 6°, this corresponding to 1290 measurements. Each diffraction pattern was recorded for 400 ms. Taking into consideration the dead time and stage movement time each slice was acquired in ~600 s. The samples yielded powder ring data and these were radially integrated (using the datasqueeze software and LaB_6 as a calibrant) for each measurement performed [31]. For each observed intensity value (I_{OBS}) in these radially integrated patterns (i.e. for all 2θ's) a sinogram was constructed and then back-projected to a 43 × 43 pixel image. For N values of 2θ, this yielded N real space reconstructed images. It follows that any vector perpendicular to such a stack of images will yield a reconstructed diffraction pattern corresponding to the selected volume element in the slice. This approach is illustrated in Fig. S1 in the Electronic Supplementary Information. Features were extracted from these reconstructed diffraction patterns that are presented herein. The processing and analysis of the considerable volume of diffraction data collected (over 50,000 diffraction patterns) required the development of dedicated high-throughput software [27].

XRD/XAFS maps of a pre-bisected and microtomed cross section (100 μm thick) were recorded on the Dutch–Belgian beamline (DUBBLE; BM26A) at the ESRF [32]. The sample was mounted on an X–Z stage with a pinhole placed before the sample to create a 200 × 200 μm square beam. The beam was then rastered across the sample by moving the X–Z stage in 200 μm steps across and down the sample and recording an XRD pattern and XAFS spectra at each point (pixel). Using an Si(111) double crystal monochromator, XRD data were collected at a wavelength of 1.40 Å, well below the Cu K-edge (1.38 Å) to avoid fluorescence effects. The Mythen detector was calibrated using a NBS silicon standard, and a 10-μm-thick Cu foil was used to calibrate the monochromator position (8979 eV). Both XRD and XAFS data were collected in transmission mode. A typical spectrum/pattern was collected more than a period of 3 min. The XAFS data were background-corrected using Athena (IFFEFIT software package) [33,34]. The normalized data were k^3-weighed and a least squares fitting analysis was performed in a k-range of 2.8 (or 3)–10 $Å^{-1}$. The Fourier transform (FT) of the k^3-weighed data was phase corrected and fit to the proposed theoretical model using the DL-EXCURV program. An amplitude reduction factor (S_o^2) value of 0.9 was used for all datasets with the R-factor being used as a determinant for the best fit [35]. The EXAFS data (300 spectra) were analyzed in batch mode (using bespoke software) to extract details on the Cu–'O' and Zn–'O' bond distances [36]. A simplified model assuming only Cu/Zn–O scattering pairs was used to fit the multiple datasets whereby any increase in Cu/Zn–O distance was taken to correspond to the formation of a Cu/Zn–S bond, respectively. A Cu/Zn–O distance then of 2.20 Å from the EXAFS refinement actually corresponds to a Cu/Zn–S distance of ~2.35 Å typical of either Cu/ZnS/Cu_2S when Cu/Zn–S scattering pairs are considered in the EXAFS (note the bond distances for the 2 copper sulfides are too similar for EXAFS to be able to distinguish between them) [37,38]. Using a Vegard relationship (Eq. (1)), it is possible to propose a percentage of Cu/ZnO vs. Cu/ZnS [39].

$$R_1\alpha + R_2(1-\alpha) = R \quad (1)$$

where R_1 = Cu/Zn(II)–O distance of 1.95 Å and where R_2 = Cu/Zn(I/II)–O(S) distance of 2.20 Å. Note that only bond distances were extracted from the sample due to problems with the sample uniformity coupled with the multiphasic nature of the catalyst material under investigation would render this information less meaningful.

$Cu/ZnO/Al_2O_3$ commercial catalysts comprising ZnO (25–35%), Al_2O_3 (5–10%), synthetic graphite (1–5%), MgO (1–-5%), and remainder CuO (45–68%) with a 5.5 mm diameter were used in this investigation. The fresh catalysts were loaded as received into a quartz tube (see Fig. S2). Each catalytic test experiment utilized 5 pellets loaded vertically into the reactor, separated by ~2 mm ceramic spheres to help reduce bypass of the sample by the reactant gases. The samples were pre-treated in a 2% H_2 in N_2 gas mix flowing at 100 ml/min during a temperature ramp from 25 to 225 °C at 0.5 °C/min with a final dwell for 1 h.

Deactivation during the WGS reaction (Eq. (2)) was performed using 3 different concentrations of H_2S; 200, 350, and 500 ppm (see Table 1). The concentrations of sulfur used were significantly higher than those encountered in a real industrial reactor but ideal for effecting accelerated sulfur poisoning. These experiments were performed at 175 °C under equal concentrations of CO and CO_2 (4 ml/min), with 20 ml/min H_2 and 16% H_2O using N_2 as a carrier gas. A repeat of the low H_2S concentration (200 ppm) experiment was performed on a crushed pellet with a sieve fraction of between 212 and 425 μm.

$$CO_{(g)} + H_2O_{(g)} \rightarrow CO_{2(g)} + H_{2(g)} \quad (2)$$

On completion of the catalyst testing, samples were recovered from the reactor after first undergoing the following passivation procedure: initial switch at 175 °C to 2% H_2 in N_2 gas mix flowing at 100 ml/min during cool down to 30 °C and hold for 1 h. The composition was then changed to 0.5% O_2, 1.5% H_2 in N_2 followed by a dwell for 1 h before the [O_2] was increased stepwise by 0.5% increments (with 1 h dwell times) up until 2% O_2 before finally being flushed with air.

3. Results

3.1. Catalytic testing

Catalytic testing of the WGS reaction performed at 175 °C over the 5.5 mm-sized $Cu/ZnO/Al_2O_3$ catalyst bodies demonstrated an increasing effect of H_2S partial pressure on activity. The presence of H_2S leads to a monotonous decrease in activity with time – see Fig. 1. After 80 h time on stream (TOS) with 200 ppm H_2S, the conversion of CO dropped to just above 30% CO conversion, whereas with 500 ppm H_2S, the sample was almost completely deactivated; complete deactivation being achieved after 95 h. Higher [H_2S] in the feed gas leads to faster deactivation. To determine the effect of catalyst form on the rate of deactivation, the same catalyst was also tested after crushing, using 200 ppm H_2S. Higher overall CO conversion is seen for the crushed sample, probably due to reduced bypass in the packed bed reactor configuration. A similar reaction profile was observed with an initial drop in activity followed by a slower deactivation. Considering that the higher overall conversion for the crushed sample is probably due to reduced bypass, the rate of deactivation appeared very similar to that of the catalyst body tested under the same catalytic conditions. The similarity in the rate of deactivation for the catalyst body and the crushed sample treated with 200 ppm H_2S suggested a similar deactivation mechanism involving an initial reaction of the H_2S with the catalyst surface followed by a slow phase change caused by the reaction of H_2S with the initial $Cu/ZnO/Al_2O_3$ components.

3.2. XRD-computed tomography catalyst characterization

The data shown in Fig. 2 represent all of the summed XRD data recorded from an entire 2D cross section of the sample, acquired as depicted in Fig. S1, after reduction in H_2 and after performing the WGS reaction in the presence of increasing amounts of H_2S. The reduced sample, as expected, was dominated by contributions ascribable to metallic face-centered cubic (fcc) Cu (111, 200, 220, 311 and 222 reflections @ 3.90°, 4.51°, 6.37°, 7.48° and 7.81° 2θ, respectively) and ZnO (100, 002, 101, 102, 110, 103 (200), 112 and 201 @ 2.90°, 3.13°, 3.29°, 4.26°, 5.01°, 5.51° (5.79°), 5.91° and 5.99° 2θ, respectively). For samples reacted in the presence of H_2S, reflections for the metallic fcc Cu phase and ZnO were still present although were much reduced in intensity – the extent of reduction decreasing with the increased amounts of H_2S in the reactant stream. This can be more clearly observed in Fig. S3. In their place reflections appeared due to CuS (Covellite *P6₃/mmc*) (102, 103, 006, 110, 116) reflections present at 2.68°, 2.91°, 3.00°, 4.30°, 5.25° 2θ) and β-ZnS (Sphalerite *F-43m*) (111, 200, 220, 311 and 331) @ 2.62°, 3.00°, 4.26°, 5.00°, 6.56° 2θ and Cu_2S (Chalcocite high *P6₃/mmc*) (100, 002, 101, 102, 110, 103) with reflections at 2.68°, 2.91°, 3.00°, 4.30°, 5.25° 2θ [37,40]. The reflection intensities for CuS(103) and β-ZnS(111) both increased with greater [H_2S], although that for Cu_2S remained similar. Note that no evidence could be found for the presence of Wurtzite (α-ZnS) in any of the sample data. The amount of CuO present in the sample increased between 200 and 350 ppm [H_2S], although decreased between 350 and 500 ppm. An additional, albeit weak but constant signal, could also be seen in all samples at 2.30° 2θ after H_2S exposure, which can be attributed to the (210) reflection of $CuSO_4$.

In order to determine the spatial distribution of the phases present in the catalyst body samples, 2D intensity distribution maps were produced using the following "diagnostic" reflections: Cu(111), ZnO(002), CuO(111), CuS(103), Cu_2S(102), and β-ZnS(111), although the data are of sufficient quality that these maps could equally be produced by using a Rietveld phase scale

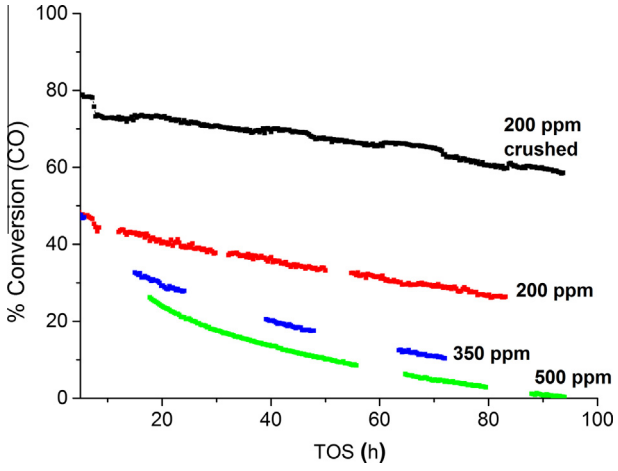

Fig. 1. Conversion of CO% at 175 °C over 5.5 mm-sized $Cu/ZnO/Al_2O_3$ catalyst bodies (also in crushed form) during the water–gas shift reaction studied for up to 100 h time on stream (TOS) in the presence of 200, 350 and 500 ppm H_2S. The gaps in the datasets represent time periods where sampling was not performed.

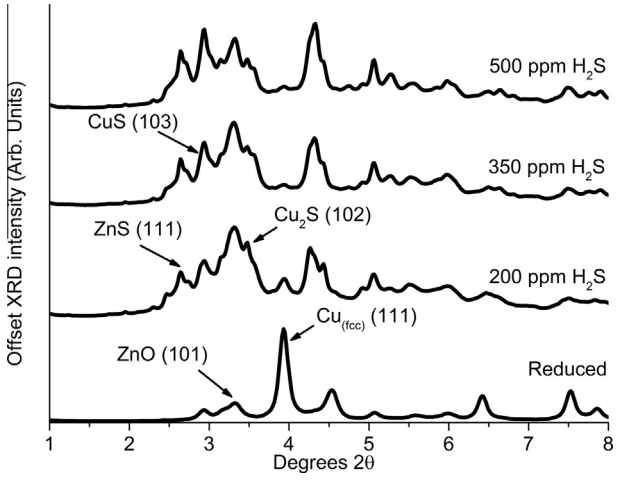

Fig. 2. 2D XRD data summed into 1D patterns for each $Cu/ZnO/Al_2O_3$ catalyst after various levels of H_2S exposure. The strongest Bragg reflections for the major phases present in the samples, including $Cu_{(fcc)}$, ZnO, Cu_2S, ZnS and CuS are indicated with arrows.

factor [41]. The color maps show the distribution of the phases presented in the 1D plot and furthermore revealed changes in 2D spatial distribution with increasing [H_2S]. The first key observations concern the phases initially present in the sample and their disappearance with increasing [H_2S] in the feed. The metallic Cu phase lost intensity and began to shrink toward the core of the catalyst body, as illustrated in Fig. 3 [42]. The distribution of CuO(1 1 1) matches closely that of the metallic Cu phase although the intensity of this signal increased between 200 and 350 ppm before being observed at its weakest and smallest (in terms of spatial distribution) at 500 ppm. This increase in CuO content between 200 and 350 ppm [H_2S] relative to the amount of metallic Cu is most likely caused by differences in the way in which the sample was oriented in the reactor which would affect H_2S uptake and the passivation process. A similar distribution/intensity profile was seen for the ZnO response (although the profiled reflection comprises a contribution for both CuO(−1 1 1) and ZnO(1 0 1)). Conversely then, the new phases that evolved possessed an inverse distribution (a broad shell around a core) to that of the initial phases with increasing [H_2S]. With increasing [H_2S], the shell of CuS and β-ZnS became thicker, concentrating further into the sample. Interestingly, the "egg-white" distribution (see Fig. S4 for an explanation) was itself non-uniform with greater signal intensity seen at the very periphery of the sample (termed an "egg–shell" distribution). Similarly, the Cu_2S phase was very much concentrated at the periphery in an egg–shell arrangement.

Representative XRD data from the 3 regions from the Cu/ZnO/Al_2O_3 catalyst body reacted in the presence of 200 ppm H_2S are given in Fig. 4. The top XRD pattern contains the summation of all XRD patterns recorded at the core (egg-yolk) of the catalyst body, the middle pattern those recorded in the corona "egg-white" region and the bottom those recorded in the peripheral "egg–shell" region. As expected, the core XRD pattern contains components assignable to metallic Cu as well as CuO and ZnO; there was no evidence for the presence of sulfur-containing phases. The summed XRD pattern recorded over the egg-white region in contrast contains components due to mainly CuS and β-ZnS and with Cu_2S being also present. Metallic Cu is not present or at least could not be clearly detected. It is important to note that due to extensive overlap of the reflections pertaining to the Cu/Zn sulfur-containing phases and those present for Cu/Zn oxides, it was not possible to rule out completely the presence of CuO/ZnO. At the periphery of the sample, the summed XRD pattern comprises a number of very sharp, well-defined reflections mostly due to Cu_2S, CuS and β-ZnS and some evidence for $CuSO_4$. The presence of very sharp, intense reflections in this region of the sample suggests a concentration of large crystalline particles, particular Cu containing species.

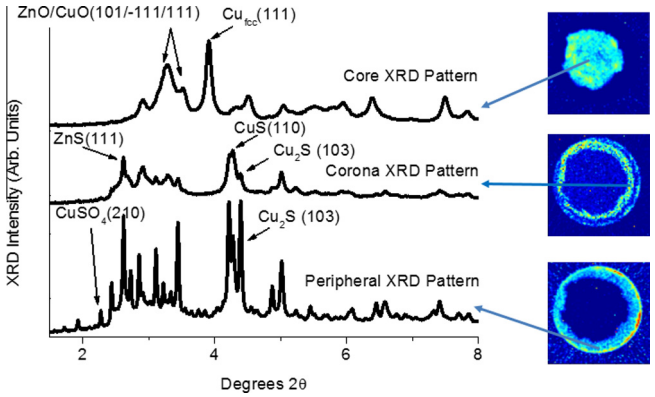

Fig. 4. Summed 1D XRD patterns (left) produced from the various regions defined (right) as core, corona and peripheral of the Cu/ZnO/Al_2O_3 catalyst body treated with 200 ppm H_2S. The major reflection for each of the various crystalline phases present in each pattern has also been identified.

3.3. X-ray fluorescence chemical mapping

In order to obtain quantitative information on the concentration/distribution of the Cu, Zn, and S components in the sample, X-ray fluorescence (XRF) data were also recorded on a bisected section of the sample reacted in the presence of 200 ppm H_2S. The results are shown in Fig. 5. It is clear that Cu was present mostly in the core and at the very edge of the sample; conversely the egg-white region of the catalyst, where the sulfur content is greatest, contains the least amount of Cu. This suggests that Cu was highly mobile in the sample, particularly in the parts of the sample where the sulfur concentration is high. Zn, on the other hand, does not appear as mobile and its distribution remains essentially uniform although there is some evidence that the signal for Zn is slightly weaker toward the sample edge (egg-white region) and that Zn depletion also occurs.

3.4. X-ray absorption chemical mapping

XRD-CT was able to identify the distribution of crystalline components over the 2D cross section and that in combination with XRF chemical mapping was able to identify heterogeneities within the catalyst bodies. However, both techniques are insensitive to the presence of small amounts of adsorbed sulfur species on the surface of metallic Cu, which have previously been implicated in catalyst deactivation (via blocking of the active site) [24]. For this purpose, chemical maps on the basis of X-ray absorption

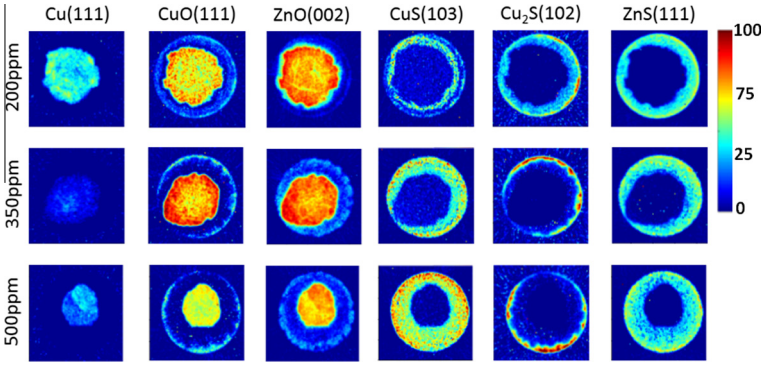

Fig. 3. 2D XRD intensity color maps produced from diagnostic reflections for the various Cu and Zn containing crystalline phases within each Cu/ZnO/Al_2O_3 catalyst body after various levels of H_2S exposure. On the right hand side is given a thermal scale bar to indicate that the intensities in each map have been scaled to the maximum and minimum values for the data presented since the absolute values for each phase vary. (For interpretation of the references to color in this figure legend, the reader is referred to the web version of this article.)

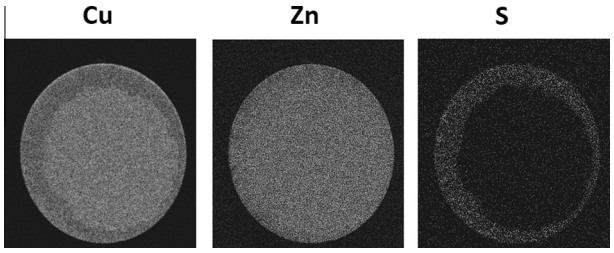

Fig. 5. Qualitative XRF maps for Cu, Zn and S recorded on a bisected section of the $Cu/ZnO/Al_2O_3$ catalyst body treated with 200 ppm H_2S. Note the darker the region, the lower the signal intensity. Cu then appears concentrated around the edge and in the middle (egg-yolk) of the sample, while Zn appears largely uniform and S is concentrated at the sample corona.

spectroscopy on a quarter of a microtomed section of the $Cu/ZnO/Al_2O_3$ catalyst body treated with 200 ppm H_2S were also measured. Alternate XRD/XAFS measurements were performed and the results obtained from an analysis of both datasets are given in Fig. 6 (Cu K-edge EXAFS) and in Figs. S5 (Zn K-edge EXAFS) and S7 (XRD). Starting with the XRD data the resultant 2D XRD phase distribution maps (Fig. S7) confirms the observations made using XRD-CT and XRF in which the CuO/ZnO phases are concentrated in the middle of the sample, whereas the sulfur-containing species (CuS, Cu_2S, and ZnS) are concentrated toward the corona and periphery of the catalyst body. The results of the EXAFS fitting of the Cu and Zn K-edge data in the form of average bond distance are summarized in Figs. 6 and S5, respectively. The Cu bond distance is <2 Å at the core and >2.1 Å toward the edge consistent with the presence of CuO at the core and CuS at the edge of the catalyst body. No evidence could be found for Cu–Cu contributions in the sample at 2.54 Å. The coordination number is observed to decrease from between 3 and 3.5 → 2 toward the edge of the catalyst body, consistent with the formation of Cu–S. For Zn–'O', the bond distance tends toward being >2.1 Å at the very edge of the catalyst body and between 1.90 and 2.0 Å toward the interior, consistent with a distribution of β-ZnS at the edge of the sample and with ZnO toward the core [43,44]. Using the Vegard relationship (Eq. (1)), it is possible to display these date in the form of a phase

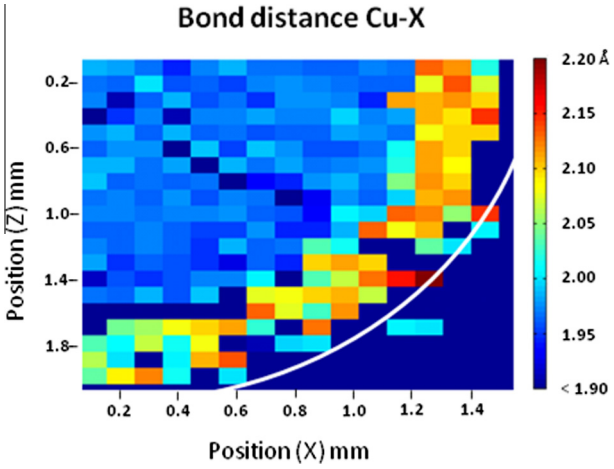

Fig. 6. Fitted EXAFS data derived Cu–'O' bond distance map of a microtomed cross section of a $Cu/ZnO/Al_2O_3$ catalyst body treated with 200 ppm H_2S. Due to time limitation only ¼ of the sample cross section has been mapped. The edge of the sample is indicated with a solid white line. The values associated with the dark blue pixels inside the sample originate because of poor data quality due to cracks in the sample. The corresponding Zn K-edge data and XRD data are given in Figs. S5 and S7. (For interpretation of the references to color in this figure legend, the reader is referred to the web version of this article.)

composition map across the sample which illustrates the presence of Cu/Zn–S species some 0.6–0.8 mm in from the edge of the sample. Beyond that (moving toward the sample core), no sulfur species were detected. Thus, the XAFS maps appear very much in agreement with the XRD-CT and XRF data where the core of the catalyst body remained sulfur-free while the exterior became laden with sulfur-containing phases.

4. Discussion

The effects of the concentration of H_2S in the feed on the WGS activity of commercial $Cu/ZnO/Al_2O_3$ catalyst bodies have been examined and the intact spent catalysts have been characterized using ex situ XRD-CT, XAFS/XRD, and XRF chemical imaging methods to determine the effects of [H_2S] on the catalyst structure. H_2S is shown to have a significant effect on the WGS activity with increasing [H_2S] leading to faster deactivation. This can be directly correlated with the formation of crystalline sulfur-containing phases. All samples exposed to H_2S contained zones of sulfur-containing phases distributed from the sample periphery and heading inwards toward the sample center; the sulfur-containing phases concentrated in an egg-white distribution, while the un-sulfided Cu(O)/ZnO phases remained intact in the center of the sample (egg-yolk distributed). The width of the egg-white component grew with increasing [H_2S], leading to a "shrinking core" of active Cu/ZnO, i.e., the size/extent of this zone decreased with increasing [H_2S] (when reaction time was constant). We estimate that for the sample poisoned using 500 ppm H_2S, >80% of the cylinder volume is converted into sulfide-containing phases. Both XRD-CT and XAFS mapping showed that the egg-white region contained a mixture of both sulfided and un-sulfided phases, including CuS, Cu_2S and $CuSO_4$ and β-ZnS, respectively. Conversely, in the center of the sample (egg-yolk region), no evidence for the presence of sulfur-containing phases could be found.

The sulfur-containing phases also exhibited different spatial distributions with XRD-CT revealing that Cu_2S and $CuSO_4$ to be located predominantly at the very edge of the samples (more egg–shell like), whereas CuS and β-ZnS are more appropriately described as egg-white. However, within this egg-white distribution, it was clear that CuS and β-ZnS were concentrated mostly at the sample periphery. The presence of more sulfided material at the sample edge was unsurprising given the previously reported capacity of Cu/ZnO systems to act as H_2S adsorbers [45]. The cause of this accumulation at the edge was, however, different for the two metals. For β-ZnS, the increased reflection intensity and FWHM of the (1 1 1) reflection in the egg–shell region in comparison with the egg-white region, as illustrated in Fig. S8, were consistent with the consumption of ZnO to form β-ZnS followed by sintering. For Cu, however, the XRF chemical maps revealed a depletion of the Cu signal in the egg-white region and enrichment in the egg–shell region suggesting that, in addition to direct consumption of metallic Cu to form copper sulfide phases and sintering, migration must have also taken place. Based on CuS having a lower melting point (500 °C) than Cu_2S (1130 °C), we propose that CuS species are the most likely candidates to exhibit mobility, migrating to the periphery under the hydrothermal conditions in which the WGS reaction was performed and that latterly Cu_2S (and $CuSO_4$) formed as a result of thermal decomposition in an O_2 containing atmosphere during the passivation process as has been previously observed [46,47]. The two copper sulfide phases present constitute the end members of the Chalcocite series of minerals (where Cu:S = 2–1) and through thermal decomposition CuS might normally be expected to yield $Cu_{1.8}S$ (Digenite) as an intermediate phase. The fact that this phase was not seen suggested that passivation was highly exothermic with temperatures

Table 1
Experimental conditions used for examining the effect of increasing [H_2S] on the WGS activity of Cu/ZnO pellets. Unless otherwise stated values are given in flow (ml/min).

Reactant gas composition/experiment	200 ppm Flow (ml/min)	350 ppm	500 ppm	200 ppm Crushed
CO	4	4	4	4
CO_2	4	4	4	4
H_2	20	20	20	20
H_2S	0.016	0.028	0.04	0.03
Total flow (with N_2 balance)	80	80	80	80
H_2O (% age)	16	16	16	16

at the sample periphery reaching in excess of 220 °C [46,48]. β-ZnS, by virtue of possessing a higher melting point (1185 °C), is not mobile and hence the distribution of Zn as observed by XRF remained largely uniform. We then interpret the sulfur XRF chemical maps in terms of β-ZnS at the corona and unreacted ZnO in the center of the sample. The formation of sulfide phases at the sample edges appeared then highly detrimental to the catalytic activity since it appeared that the catalyst became inactive before all Cu/ZnO had been sulfided. This suggested that the formation of Cu/Zn sulfided phases may also affect catalyst porosity leading to inhibited diffusion via pore blocking by mobile sulfides or through destruction of the internal pore structure during the formation of the sulfide phases. The similarity of the deactivation profile seen for the smaller particles used in the crushed sample suggested that the mechanism of deactivation (formation of sulfides) was not affected by the type of flow-regime employed i.e. single-pellet-string or plug-flow reactor.

5. Concluding remarks

Industrial Cu/ZnO/Al_2O_3 catalysts are unlikely to see anything like the amount of H_2S used in this study; however, the tendency for Cu and Zn to adsorb S does mean that, over time, sulfide phases will accrue in much the same way as we observed here. In addition, while passivation is not a typical experience of an industrial catalyst, regeneration in air/oxygen is a similar yet more vigorous process that the catalyst experiences and thus the phase evolution, migration we observed may also occur in real samples. Ideally, future studies would be best performed in situ so as to decouple the stages of the initial and subsequent sulfide formation should effective strategies to combat S-poisoning result. As illustrated here, however, it is important to consider the spatial component when trying to determine the structure-activity relationships in real heterogeneous catalyst samples [49–54]. The development and utilization of imaging methods are critical therefore for such purposes [55].

Acknowledgments

The authors acknowledge ACTS-ASPECT (NWO) and EPSRC (UK) for funding and ESRF for beamtime.

Appendix A. Supplementary material

Supplementary data associated with this article can be found, in the online version, at http://dx.doi.org/10.1016/j.jcat.2014.04.007.

References

[1] H.F. Rase, Handbook of Commercial Catalysts, CRC Press, Boca Raton, 2000.
[2] J. Hagen, Industrial Catalysts, A Practical Approach, Wiley-VCH, Weinheim, 1999.
[3] M.E. Baerns, Basic Principles in Applied Catalysis, Springer, Berlin, 2004.
[4] J.A. Moulijn, A.E. van Diepen, F. Kapteijn, G. Ertl, H. Knozinger, F. Schuth, J. Weitkamp (Eds.), Handbook of Heterogeneous Catalysis, second ed., Wiley-VCH, Weinheim, 2008.
[5] J.A. Moulijn, A.E. van Diepen, F. Kapteijn, Appl. Catal. A 212 (2001) 3–16.
[6] S.Y. Jung, S.C. Lee, H.K. Jun, J.C. Kim, Catal. Surv. Asia 17 (2013) 85–102.
[7] X. Meng, W. de Jong, R. Pal, A.H.M. Verkooijen, Fuel Process. Technol. 91 (2010) 964–981.
[8] A. Demirbas, Prog. Energ. Combust. Sci. 31 (2005) 171–192.
[9] M.S. Spencer, M.V. Twigg, Annu. Rev. Mater. Res. 35 (2005) 427–464.
[10] M. Behrens, F. Studt, I. Kasatkin, S. Kuehl, M. Haevecker, F. Abild-Pedersen, S. Zander, F. Girgsdies, P. Kurr, B.-L. Kniep, M. Tovar, R.W. Fischer, J.K. Norskov, R. Schloegl, Science 336 (2012) 893–897.
[11] X.M. Liu, G.Q. Lu, Z.F. Yan, J. *Ind. Eng. Chem. Res.* 42 (2003) 6518–6530.
[12] M.V. Twigg, M.S. Spencer, Top. Catal. 22 (2003) 191–203.
[13] B.S. Clausen, H. Topsoe, Catal. Today 9 (1991) 189–196.
[14] P.L. Hansen, J.B. Wagner, S. Helveg, J.R. Rostrup-Nielsen, B.S. Clausen, H. Topsoe, Science 295 (2002) 2053–2055.
[15] M.V. Twigg, M.S. Spencer, Appl. Catal. A 212 (2001) 161–174.
[16] C. Guoyong, A. Dagang, L. Chengyue, in: C.H. Bartholomew, J.B. Butt (Eds.), Catalyst Deactivation, Elsevier, Amsterdam, 1991.
[17] M.S. Spencer, Top. Catal. 8 (1999) 259–266.
[18] J. Baars, G. Brandt, J. Phys. Chem. Solids 34 (1973) 905–909.
[19] H.-T. Kim, S.-M. Kim, K.-W. Jun, Y.-S. Yoon, J.-H. Kim, Int. J. Hydrogen Energ. 32 (2007) 3603–3608.
[20] J. Skrzypski, I. Bezverkhyy, O. Heintz, J.-P. Bellat, Ind. Eng. Chem. Res. 50 (2011) 5714–5722.
[21] S.-H. Kang, J.W. Bae, S.-M. Kim, K.-W. Jun, Energy Fuels 22 (2008) 2580–2584.
[22] B.J. Wood, W.E. Isakson, H. Wise, Ind. Eng. Chem. Prod. RD. 19 (1980) 197–204.
[23] A.F. Carley, P.R. Davies, R.V. Jones, K.R. Harikumar, G.U. Kulkarni, M.W. Roberts, Surf. Sci. 447 (2000) 39–50.
[24] A.F. Carley, P.R. Davies, R.V. Jones, K.R. Harikumar, M.W. Roberts, Chem. Commun. (2000) 185–186.
[25] L. Moroney, S. Rassias, M.W. Roberts, Surf. Sci. 105 (1982) L249–L254.
[26] L. Espinosa-Alonso, A.M. Beale, B.M. Weckhuysen, Acc. Chem. Res. 43 (2010) 1279–1288.
[27] S.D.M. Jacques, M. Di Michiel, A.M. Beale, T. Sochi, M.G. O'Brien, L. Espinosa-Alonso, B.M. Weckhuysen, P. Barnes, Angew. Chem. Int. Ed. 50 (2011) 10148–10152.
[28] M.G. O'Brien, S.D.M. Jacques, M. Di Michiel, P. Barnes, B.M. Weckhuysen, A.M. Beale, Chem. Sci. 3 (2012) 509–523.
[29] J. Ruiz-Martinez, A.M. Beale, U. Deka, M.G. O'Brien, P.D. Quinn, J.F.W. Mosselmans, B.M. Weckhuysen, Angew. Chem. Int. Ed. 52 (2013) 5983–5987.
[30] S.D.M. Jacques, M. Di Michiel, S.A.J. Kimber, X. Yang, R.J. Cernik, A.M. Beale, S.J.L. Billinge, Nature Commun. 4 (2013). 2536–2536.
[31] http://www.datasqueezesoftware.com/index.html.
[32] S. Nikitenko, A.M. Beale, A.M.J. van der Eerden, S.D.M. Jacques, O. Leynaud, M.G. O'Brien, D. Detollenaere, R. Kaptein, B.M. Weckhuysen, W. Bras, J. Synchrotron. Radiat. 15 (2008) 632–640.
[33] M. Newville, J. Synchrotron. Radiat. 8 (2001) 322–324.
[34] B. Ravel, M. Newville, J. Synchrotron. Radiat. 12 (2005) 537–541.
[35] J.G. Mesu, T. Visser, F. Soulimani, E.E. van Faassen, P. de Peinder, A.M. Beale, B.M. Weckhuysen, Inorg. Chem. 45 (2006) 1960–1971.
[36] A.M. Beale, A.M.J. van der Eerden, K. Kervinen, M.A. Newton, B.M. Weckhuysen, Chem. Commun. (2005) 3015–3017.
[37] Y. Takeuchi, Y. Kudoh, G. Sato, Zeitschrift Fur Kristallographie 173 (1985) 119–128.
[38] R.J. Cava, F. Reidinger, B.J. Wuensch, Solid State Ionics 5 (1981) 501–504.
[39] H. Kajiyama, S. Muramatsu, T. Shimada, Y. Nishino, Phys. Rev. B 45 (1992) 14005–14010.
[40] M.K. Rabadanov, A.A. Loshmanov, Y.V. Shaldin, Kristallografiya 42 (1997) 649–659.
[41] C.K. Egan, S.D.M. Jacques, M. Di Michiel, B. Cai, M.W. Zandbergen, P.D. Lee, A.M. Beale, R.J. Cernik, Acta Biomater. 9 (2013) 8337–8345.
[42] K.Y. Cheah, N. Chiaranussati, M.P. Hollewand, L.F. Gladden, Appl. Catal. A. 115 (1994) 147–155.
[43] C. Priadi, P. Le Pape, G. Morin, S. Ayrault, F. Maillot, F. Juillot, R. Hochreutener, I. Llorens, D. Testemale, O. Proux, G.E. Brown Jr., Environ. Sci. Technol. 46 (2012) 3712–3720.
[44] K. Tohji, Y. Udagawa, T. Mizushima, A. Ueno, J. Phys. Chem. 89 (1985) 5671–5676.
[45] P. Dhage, A. Samokhvalov, M.L. McKee, E.C. Duin, B.J. Tatarchuk, Surf. Interface Anal. 45 (2013) 865–872.
[46] J.G. Dunn, C. Muzenda, Thermochim. Acta 369 (2001) 117–123.
[47] E. Godocikova, P. Balaz, J.M. Criado, C. Real, E. Gock, Thermochim. Acta 440 (2006) 19–22.

[48] Q.-L. Huang, H. Chen, Y.C. Zhang, C.L. Wu, J. Alloy Compd. 509 (2011) 6382–6387.
[49] A. Urakawa, A. Baiker, Top. Catal. 52 (2009) 1312–1322.
[50] A.M. Beale, S.D.M. Jacques, B.M. Weckhuysen, Chem. Soc. Rev. 39 (2010) 4656–4672.
[51] I.L.C. Buurmans, B.M. Weckhuysen, Nature Chem. 4 (2012) 873–886.
[52] J.D. Grunwaldt, C.G. Schroer, Chem. Soc. Rev. 39 (2010) 4741–4753.
[53] J.-D. Grunwaldt, J.B. Wagner, R.E. Dunin-Borkowski, Chemcatchem 5 (2013) 62–80.
[54] C.G. Schroer, J.-D. Grunwaldt, J.A. Rodriguez, J.C. Hanson, P.J. Chupas (Eds.), In-Situ Characterization of Heterogeneous Catalysts, Wiley-VCH, Mannheim, 2013.
[55] S. Mitchell, N.-L. Michels, J. Perez-Ramirez, Chem. Soc. Rev. 42 (2013) 6094–6112.